

Potential-energy gating for robust state estimation in bistable  
stochastic systems

Luigi Simeone<sup>1</sup>

<sup>1</sup>*Independent Researcher, Turin, Italy\**

(Dated: February 13, 2026)

## Abstract

We introduce potential-energy gating, a method for robust state estimation in systems governed by double-well stochastic dynamics. The core idea is to modulate the observation noise covariance of a Bayesian filter using the local value of a known or assumed potential energy function: observations are trusted when the state sits near a potential minimum and progressively discounted as the state approaches the barrier separating metastable wells. This physics-based mechanism differs from purely statistical robust filters, which treat all regions of state space identically, and from constrained filters, which impose hard bounds on the state rather than modulating observation trust. We implement the gating within Extended, Unscented, Ensemble, and Adaptive Kalman filters as well as particle filters, requiring only two additional hyperparameters beyond the standard formulation. Synthetic benchmarks on a Ginzburg-Landau double-well process with 10% outlier contamination and Monte Carlo validation over 100 independent replications show that potential-energy gating improves root-mean-square estimation error by 57–80% relative to the standard Extended Kalman Filter, with all improvements statistically significant ( $p < 10^{-15}$ , Wilcoxon signed-rank test). A naive topological baseline that uses only the distance to the nearest well—without the potential energy profile—achieves 57% improvement, confirming that the continuous energy landscape contributes an additional  $\sim 21$  percentage points. The method is robust to parameter misspecification: even when the assumed potential parameters deviate by 50% from their true values, the improvement never falls below 47%. A supplementary comparison between externally forced and spontaneous (Kramers-type) transitions shows that the gating mechanism retains 68% improvement under noise-induced transitions, whereas the naive baseline degrades to 30%. As an empirical illustration, we apply the framework to Dansgaard-Oeschger events in the NGRIP  $\delta^{18}\text{O}$  ice-core record, estimating an asymmetry parameter  $\gamma = -0.109$  (bootstrap 95% CI:  $[-0.220, -0.011]$ , excluding zero) and demonstrating that outlier fraction explains 91% of the variance in filter improvement.

---

\* [luigi.simeone@tech-management.net](mailto:luigi.simeone@tech-management.net)

## I. INTRODUCTION

Bistable stochastic systems—processes whose dynamics are governed by a double-well potential energy landscape—arise across the physical, biological, and social sciences [1]. Examples include Josephson junctions in condensed matter physics [2], gene regulatory switches in molecular biology [3], abrupt climate transitions in paleoclimatology [4], and regime-switching dynamics in quantitative finance [5]. In all these systems, the coexistence of two metastable states separated by an energy barrier creates a fundamental challenge for state estimation: during transitions between wells, observations become unreliable because the system traverses a region of high potential energy where the restoring force vanishes and noise dominates the dynamics.

Standard Bayesian filtering—the Extended Kalman Filter (EKF) and its variants [6, 7]—treats observation noise as homogeneous across state space. When the observation channel is contaminated by outliers (measurement errors whose magnitude exceeds typical process fluctuations), this assumption leads to catastrophic state estimate corruption, because the filter cannot distinguish a legitimate transition between wells from an anomalous measurement. Existing approaches to outlier-robust filtering fall into three categories, none of which exploits the physics of the energy landscape.

First, *statistical gating* methods, such as chi-square gating based on the Mahalanobis distance [8, 9], reject observations that are statistically surprising according to the filter’s own innovation covariance. This mechanism is binary (accept or reject), physics-agnostic, and fails precisely when it is needed most: during genuine transitions, the innovation is large *because* the state is changing, so statistical gating may reject valid measurements.

Second, *heavy-tailed filters* replace Gaussian noise assumptions with Student- $t$  distributions [10–12], providing soft down-weighting of outlying observations. While effective for uniformly contaminated data, these methods apply the same degree of robustness everywhere in state space, with no mechanism to exploit the fact that observations near well minima are physically more reliable than observations near the barrier.

Third, *regime-switching models* [5] and the Interacting Multiple Model (IMM) algorithm [13] assign discrete labels to regimes and switch between parameter sets. These approaches impose a discrete, finite number of states rather than a continuous energy landscape, and the switching probabilities are typically estimated from data rather than derived

from physics.

The present work proposes a fourth approach: *potential-energy gating*, in which the observation noise covariance  $R$  is modulated by the local value of a known or assumed potential energy function  $V(x)$ . When the state estimate  $\hat{x}$  sits near a potential minimum ( $V(\hat{x}) \approx 0$ ), observations are trusted at their nominal uncertainty  $R_0$ . As  $\hat{x}$  moves toward the barrier ( $V(\hat{x}) \rightarrow V_{\max}$ ), the effective observation noise is inflated:

$$R_{\text{eff}}(x) = R_0 \cdot [1 + g V(x)], \quad (1)$$

where  $g > 0$  is a gating sensitivity parameter. This mechanism is continuous, state-dependent, and physics-based: it encodes the physical intuition that observations of a system traversing an unstable equilibrium carry less information about the underlying state than observations of a system resting in a metastable well.

### A. Relation to prior work

The use of double-well potentials for modeling abrupt climate transitions has a rich history. Ditlevsen [4] established the paradigm of Dansgaard-Oeschger (D-O) events as noise-induced transitions in a bistable potential, fitting a Langevin model to the GRIP  $\text{Ca}^{2+}$  record. Kwasniok and Lohmann [14] used the Unscented Kalman Filter (UKF) for maximum-likelihood estimation of double-well SDE parameters from the NGRIP  $\delta^{18}\text{O}$  record, while Kwasniok [15] extended this framework to disentangle dynamical and observational noise using predictive likelihood maximization. Livina, Kwasniok, and Lenton [16] developed potential analysis—fitting polynomial potentials to empirical probability densities—to detect changes in the number of climate states over the last 60 kyr. Livina and Lenton [17] proposed bifurcation detection via detrended fluctuation analysis as an early-warning signal. Lohmann and Ditlevsen [18] used Approximate Bayesian Computation to compare double-well and relaxation oscillator models, finding evidence favoring the oscillator for D-O dynamics.

All of these contributions address the *inverse problem*: reconstructing the potential from data. Our work addresses a different and complementary question—the *forward problem* of using a known or assumed potential to improve real-time state estimation. The Kalman filter in Kwasniok’s work serves as a parameter estimation engine; in our framework, the

filter is the end product, and the potential serves as prior physical knowledge that modulates its observation model.

In the broader context of physics-informed inference, constrained Kalman filtering [19] imposes hard bounds on the state vector but does not modify the observation model. Physics-informed neural networks (PINNs) [20, 21] embed PDE residuals in training loss functions but operate in batch mode rather than sequential filtering. Data-driven methods such as SINDy [22] discover governing equations from data but require high-frequency, low-noise sampling. Adaptive methods for jointly estimating model and observation error covariances [23] infer  $R$  from the statistical properties of innovation sequences rather than prescribing it from physics. The present approach is, to our knowledge, the first to embed physics in the *observation reliability channel* of a Bayesian filter: modulating  $R$  rather than constraining  $x$  or regularizing the process model.

## B. Scope and organization

This paper is methodological in scope. We propose and validate a general mechanism—potential-energy gating—for any system whose dynamics can be approximated by a double-well potential. The NGRIP paleoclimatic application in Sec. V serves as an empirical illustration of how the method can be applied to real data, not as a claim about the optimal model for D-O events. We explicitly acknowledge the work of Lohmann and Ditlevsen [18], which has shown that a relaxation oscillator model may outperform the simple double-well for D-O dynamics; our use of the Ginzburg-Landau potential for NGRIP is intended to demonstrate the gating mechanism on a well-known dataset, not to argue that the quartic potential is the best physical model for this system.

The paper is organized as follows. Section II defines the state-space model and the Ginzburg-Landau potential. Section III derives the potential-gated filter. Section IV presents synthetic validation, including Monte Carlo benchmarks, misspecification analysis, and the naive topological baseline. Section V applies the framework to NGRIP data. Section VI discusses limitations and Sec. VII concludes.

## II. STATE-SPACE MODEL AND POTENTIAL ENERGY

### A. Continuous-time dynamics

We consider a scalar state  $x(t) \in \mathbb{R}$  evolving according to the overdamped Langevin equation

$$dx = -V'(x) dt + \sigma dW, \quad (2)$$

where  $V(x)$  is a confining potential,  $\sigma > 0$  is the noise intensity, and  $W(t)$  is a standard Wiener process. The drift term  $-V'(x)$  drives the state toward local minima of  $V$ ; the noise term  $\sigma dW$  drives fluctuations and, over sufficiently long times, transitions between wells.

### B. The Ginzburg-Landau potential

We parametrize  $V(x)$  using the Ginzburg-Landau (GL) form [24], the minimal polynomial potential that exhibits bistability. In its symmetric version [Eq. (3)],

$$V(x) = -\frac{\alpha}{2} x^2 + \frac{\beta}{4} x^4, \quad \alpha, \beta > 0. \quad (3)$$

This potential has two degenerate minima at  $x_{\pm} = \pm\sqrt{\alpha/\beta}$ , separated by a barrier of height  $\Delta V = \alpha^2/(4\beta)$  located at  $x = 0$ . We also consider the asymmetric extension

$$V_{\gamma}(x) = V(x) - \gamma x, \quad (4)$$

where  $\gamma \in \mathbb{R}$  tilts the potential, breaking the degeneracy between the two wells. This form has been used to model the asymmetry between stadial and interstadial states in glacial climate [4, 14].

Figure 1 illustrates the symmetric and asymmetric GL potential, highlighting the wells, the barrier, and the regions where the gating mechanism modulates observation trust.

The key physical quantities are: the barrier height  $\Delta V$ , which sets the energy scale for transitions; the effective temperature  $T_{\text{eff}} = \sigma^2/2$ , which characterizes the thermal fluctuation energy; and their ratio  $\Pi_1 = \Delta V/T_{\text{eff}}$ , which governs the Kramers escape rate [2].

### Ginzburg-Landau Potential: Bifurcation from Monostable to Bistable

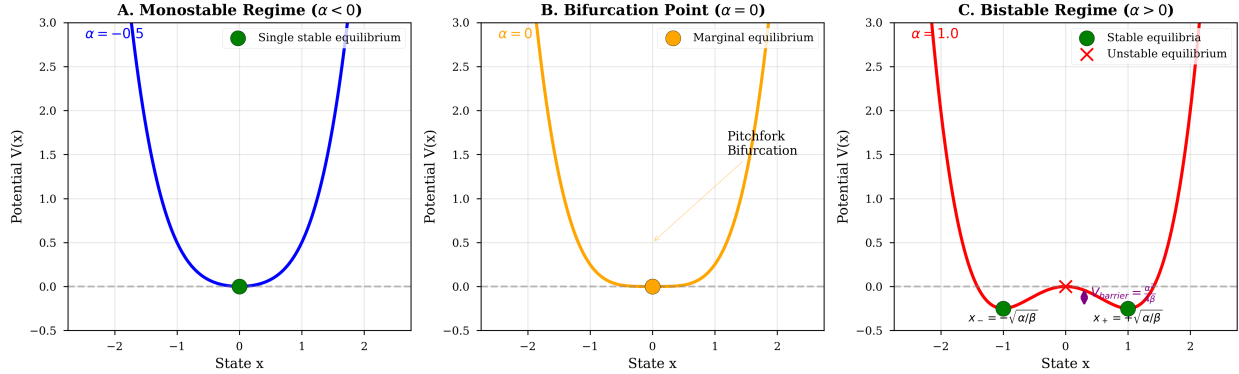


FIG. 1. The Ginzburg-Landau potential  $V(x)$  for different parameter regimes. The symmetric case ( $\gamma = 0$ ) exhibits two degenerate wells at  $x_{\pm} = \pm\sqrt{\alpha/\beta}$  separated by a barrier of height  $\Delta V = \alpha^2/(4\beta)$ . The asymmetric case ( $\gamma \neq 0$ ) tilts the landscape, making one well deeper than the other. In the potential-energy gating framework, observations are trusted near the well minima (low  $V$ ) and discounted near the barrier (high  $V$ ).

### C. Discrete-time state-space model

Discretizing Eq. (2) with time step  $\Delta t$  via the Euler-Maruyama scheme and adding an observation equation, we obtain the state-space model

$$x_{k+1} = x_k + f(x_k) \Delta t + \sigma \sqrt{\Delta t} \eta_k, \quad (5)$$

$$y_k = x_k + \varepsilon_k, \quad (6)$$

where  $f(x) = -V'(x) = \alpha x - \beta x^3 + \gamma$  is the drift,  $\eta_k \sim \mathcal{N}(0, 1)$  is the process noise, and  $\varepsilon_k$  is the observation noise [Eq. (6)]. In practice,  $\varepsilon_k$  may be heavy-tailed due to measurement errors, instrument failures, or external contamination. We model this as a mixture: with probability  $(1-p)$ ,  $\varepsilon_k \sim \mathcal{N}(0, R_0)$  (clean observation), and with probability  $p$ ,  $\varepsilon_k \sim \mathcal{N}(0, R_0 + R_{\text{out}})$  (outlier), where  $R_{\text{out}} \gg R_0$ .

### III. POTENTIAL-GATED BAYESIAN FILTERING

#### A. Motivation: energy-dependent observation reliability

The central observation motivating our approach is that in a bistable system, the *physical reliability* of an observation depends on where the system sits in the energy landscape. Near a potential minimum, the restoring force  $|f(x)|$  is large, fluctuations are bounded, and an observation provides high-quality information about the latent state. Near the barrier top, the restoring force vanishes, the system is maximally sensitive to perturbations, and an observation carries less information because it cannot distinguish the true state from noise excursions or incipient transitions.

This motivates replacing the constant observation noise covariance  $R_0$  with a state-dependent covariance, as previewed in Eq. (1):

$$R(x) = R_0 \cdot [1 + g V(x)], \quad (7)$$

where  $g \geq 0$  is the gating sensitivity. When  $g = 0$ , the standard filter is recovered. As  $g$  increases, the filter progressively discounts observations when the state estimate is in a high-energy region.

We emphasize that Eq. (7) is a *heuristic* motivated by physical intuition, not a rigorous derivation from first principles. The connection to statistical mechanics is suggestive—the Boltzmann weight  $\exp(-V/T_{\text{eff}})$  governs the stationary distribution of Eq. (2), so regions of high  $V$  are intrinsically less probable—but we do not claim a formal fluctuation-dissipation derivation. The justification for Eq. (7) is ultimately empirical: it works, and it works for physically interpretable reasons.

#### B. Regularized state update

In the standard EKF, the state update minimizes the quadratic cost

$$J_{\text{std}}(x) = \frac{(x - \hat{x}^-)^2}{P^-} + \frac{(y - x)^2}{R_0}, \quad (8)$$

where  $\hat{x}^-$  and  $P^-$  are the predicted state and covariance. We augment this cost with a physics-informed penalty term [Eq. (9)]:

$$\mathcal{H}(x) = \frac{(x - \hat{x}^-)^2}{P^-} + \frac{(y - x)^2}{R(x)} + \lambda V(x), \quad (9)$$

where  $\lambda \geq 0$  controls the strength of the potential-energy regularization and  $R(x)$  is given by Eq. (7). The updated state estimate [Eq. (10)] is

$$\hat{x}^+ = \arg \min_x \mathcal{H}(x), \quad (10)$$

obtained numerically via the L-BFGS-B algorithm [25] initialized at the standard Kalman update.

The cost function  $\mathcal{H}$  has a natural interpretation as a penalized negative log-posterior. The first term is the Gaussian prior from the prediction step, the second is the (state-dependent) log-likelihood, and the third is a Boltzmann-inspired prior that penalizes states in high-energy regions. This interpretation is approximate—the state-dependent  $R(x)$  term introduces a normalization factor that is neglected—but provides useful intuition for the role of each component.

### C. Posterior covariance via the Hessian

After optimization, the posterior covariance is estimated from the curvature of  $\mathcal{H}$  at the optimum:

$$P^+ = [\mathcal{H}''(\hat{x}^+)]^{-1}, \quad (11)$$

where the full Hessian [Eq. (12)] reads

$$\mathcal{H}''(x) = \frac{1}{P^-} + \frac{1}{R(x)} + \lambda V''(x). \quad (12)$$

For the symmetric GL potential,  $V''(x) = -\alpha + 3\beta x^2$ , which is positive at the well minima ( $V''(x_{\pm}) = 2\alpha$ ) and negative at the barrier ( $V''(0) = -\alpha$ ). The covariance is floored at  $P_{\min} = 10^{-4}$  to prevent numerical degeneracy.

This Hessian-based covariance is more consistent with the optimization-based state update than the standard Kalman covariance formula, which assumes a linear observation model and constant  $R$ . However, it tends to produce a slightly over-confident posterior, as discussed in Sec. VI C.

### D. The two hyperparameters

The method introduces exactly two hyperparameters beyond the standard filter:  $\lambda$  (regularization strength), which controls how strongly the potential energy penalty attracts the

state estimate toward well minima, with a typical range  $\lambda \in [0.01, 1.0]$ ; and  $g$  (gating sensitivity), which controls how rapidly the observation noise inflates near the barrier, with a typical range  $g \in [1, 50]$ . Section IV C demonstrates that a broad “Goldilocks zone” in  $(\lambda, g)$ -space provides near-optimal performance, reducing the need for application-specific tuning.

### E. Extension to other filter architectures

The gating mechanism is not specific to the EKF. We implement potential-gated variants of five filter families, denoted PG-EKF, PG-UKF [26], PG-AKF (Adaptive Kalman Filter), PG-EnKF [27], and PG-PF [28].

In the PG-UKF, the state update is replaced by minimization of  $\mathcal{H}$  with sigma-point weights unmodified. In the PG-AKF, the process noise  $Q_k$  is adjusted from the innovation sequence while the observation noise is gated by  $R(x)$ . In the PG-EnKF, observation perturbation noise is scaled by  $R(x)$  rather than  $R_0$ . In the PG-PF, the likelihood evaluation uses  $R(x_k^{(i)})$  for each particle  $x_k^{(i)}$ —the most natural architecture for potential-energy gating, since the particle filter already evaluates the likelihood particle-by-particle. In all cases, the standard (non-gated) version is recovered by setting  $\lambda = 0$  and  $g = 0$ .

### F. Naive topological baseline

To isolate the contribution of the *continuous potential profile* from the simpler effect of *knowing where the wells are*, we define a naive topological baseline (NT-EKF) that uses only the distance to the nearest well [Eq. (13)]:

$$R_{\text{NT}}(x) = R_0 \cdot [1 + g d_{\min}^2(x)], \quad (13)$$

where  $d_{\min}(x) = \min(|x - x_-|, |x - x_+|)$  and  $x_{\pm}$  are the well positions. This baseline inflates  $R$  quadratically with distance from the nearest well, but does not use the shape of the potential between the wells. The comparison PG-EKF vs. NT-EKF quantifies the informational value of the continuous energy landscape beyond simple topology.

## IV. SYNTHETIC VALIDATION

### A. Experimental protocol

We generate synthetic data from Eqs. (5)–(6) with parameters  $\alpha = 1$ ,  $\beta = 1$ ,  $\sigma = 0.3$ ,  $\Delta t = 1$ ,  $T = 300$  time steps, and outlier contamination probability  $p = 0.10$  with outlier scale  $R_{\text{out}} = 100 R_0$ . The trajectory includes externally forced transitions between wells to ensure that both wells are visited within the observation window; we discuss spontaneous (Kramers-type) transitions separately in Sec. IV E.

Filter hyperparameters are fixed throughout all experiments:  $\lambda = 0.1$ ,  $g = 10$ ,  $R_0 = 0.3^2$ ,  $Q = 0.3^2$ . The particle filter uses  $N_p = 500$  particles; the ensemble Kalman filter uses  $N_e = 50$  members. Performance is measured by the root-mean-square error  $\text{RMSE} = \sqrt{N^{-1} \sum_k (\hat{x}_k - x_k^{\text{true}})^2}$ .

### B. Monte Carlo benchmark

To provide statistically rigorous performance estimates, we run  $N_{\text{MC}} = 100$  independent replications, each with a different random seed controlling the process noise, observation noise, and outlier locations. Table I reports the mean RMSE, standard deviation, 95% confidence interval (mean  $\pm 1.96 \cdot \text{SE}$ ,  $\text{SE} = \text{std}/\sqrt{N_{\text{MC}}}$ ), and the  $p$ -value from a Wilcoxon signed-rank test (paired, against EKF Std). All twelve filters are tested on each replication.

Figure 2 shows the full RMSE distribution for each filter as a violin plot, providing visual confirmation that the improvements are not artifacts of outlier replications but reflect systematic shifts of the entire distribution.

Several patterns emerge from Table I and Fig. 2. Every potential-gated filter outperforms its standard counterpart, with improvements ranging from 57% (NT-EKF, which uses only topology) to 80% (PG-PF, the best overall performer). The PG-EKF achieves  $78.2\% \pm 3.5\%$  improvement with computational cost only  $13\times$  that of the standard EKF per step, making it the most efficient choice on the Pareto frontier of accuracy vs. cost. The chi-square-gated Robust EKF achieves only 37.6% improvement, demonstrating that statistical gating based on the Mahalanobis distance captures less than half the benefit of physics-based gating.

The PG-UKF warrants a note of caution. While its median RMSE (0.285) is excellent, six replications out of 100 produce  $\text{RMSE} > 1.0$ , with two extreme values at 3.67 and

TABLE I. Monte Carlo benchmark ( $N_{MC} = 100$  replications,  $N = 150$ ,  $p = 0.10$ ). Improvement is relative to EKF Std. All  $p$ -values from paired Wilcoxon signed-rank tests. PG = potential-gated; NT = naive topological baseline; Std = standard (no gating); Robust = chi-square gating.

| Filter     | RMSE (mean $\pm$ std) | 95% CI         | Impr. (%) | $p$          |
|------------|-----------------------|----------------|-----------|--------------|
| PG-PF      | $0.257 \pm 0.054$     | [0.246, 0.267] | +80.4     | $< 10^{-17}$ |
| PG-EKF     | $0.286 \pm 0.043$     | [0.277, 0.294] | +78.2     | $< 10^{-17}$ |
| PG-AKF     | $0.363 \pm 0.139$     | [0.336, 0.390] | +72.3     | $< 10^{-17}$ |
| PG-UKF     | $0.414 \pm 0.554$     | [0.305, 0.522] | +68.7     | $< 10^{-14}$ |
| PG-EnKF    | $0.444 \pm 0.076$     | [0.429, 0.459] | +66.1     | $< 10^{-17}$ |
| NT-EKF     | $0.564 \pm 0.116$     | [0.541, 0.587] | +57.0     | $< 10^{-17}$ |
| EnKF Std   | $0.731 \pm 0.128$     | [0.706, 0.756] | +44.2     | $< 10^{-17}$ |
| PF Std     | $0.731 \pm 0.036$     | [0.724, 0.738] | +44.1     | $< 10^{-17}$ |
| EKF Robust | $0.821 \pm 0.155$     | [0.790, 0.851] | +37.6     | $< 10^{-17}$ |
| UKF Std    | $0.960 \pm 0.071$     | [0.946, 0.974] | +26.8     | $< 10^{-17}$ |
| AKF Std    | $1.244 \pm 0.094$     | [1.226, 1.263] | +5.3      | $< 10^{-17}$ |
| EKF Std    | $1.313 \pm 0.080$     | [1.297, 1.329] | —         | —            |

3.85. This instability arises because UKF sigma points can fall in the barrier region where  $V''(0) = -\alpha < 0$ , causing the Hessian-based covariance (Eq. 11) to become ill-conditioned. We recommend reporting the median alongside the mean for the PG-UKF and note that this issue does not affect the EKF or PF implementations.

### C. Goldilocks zone for hyperparameters

We sweep  $\lambda \in [0.01, 2.0]$  and  $g \in [1, 50]$  over a two-dimensional grid, evaluating the PG-EKF at each point for four potential topologies ( $\alpha \in \{0.6, 1.0, 1.41, 2.0\}$ ,  $\beta = 1$ ). Figure 3 shows that a broad plateau of near-optimal performance exists for  $\lambda \in [0.05, 0.5]$  and  $g \in [5, 30]$ . Performance degrades gracefully outside this region: too-small  $\lambda$  or  $g$  recovers the standard filter, while too-large values introduce excessive bias toward well minima. Importantly, the Goldilocks zone is stable across the tested topologies, indicating that the hyperparameters do not require re-tuning for each application.

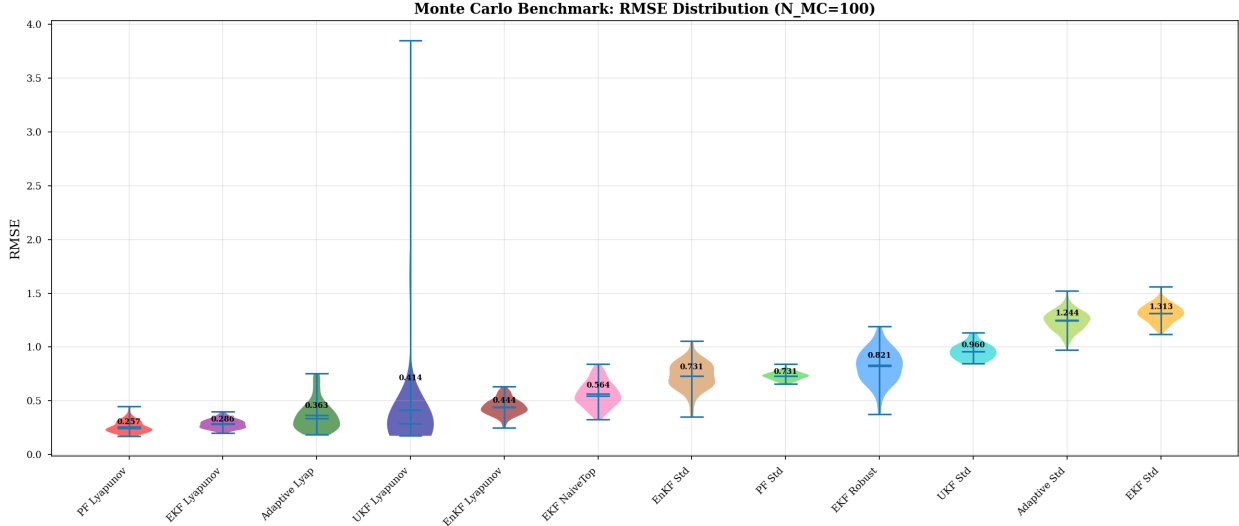


FIG. 2. Distribution of RMSE across 100 Monte Carlo replications for all twelve filters ( $N = 150$ , 10% outlier contamination). Violin bodies show kernel density estimates; horizontal bars mark means. The potential-gated filters (PG-PF through PG-EnKF) cluster at low RMSE, well separated from their standard counterparts. The NT-EKF (naive topological baseline) sits between the gated and standard groups, capturing 57% of the improvement without using the full potential profile. Note the long upper tail of PG-UKF (mean = 0.414, median = 0.285), reflecting occasional numerical instability when sigma points fall in the barrier region where  $V''(0) < 0$ .

#### D. Model misspecification analysis

A central concern for any physics-informed method is robustness to incorrect physical assumptions. We assess this by generating data with true parameters  $\alpha^* = 1.0$ ,  $\beta^* = 1.0$  and running the PG-EKF with assumed parameters on a grid  $\alpha_{\text{assumed}}, \beta_{\text{assumed}} \in \{0.5, 0.7, 0.8, 0.9, 1.0, 1.1, 1.2, 1.5\}$ , with 20 Monte Carlo replications per cell. The standard EKF, which uses no potential parameters, serves as the invariant baseline.

Figure 4 presents the results as heatmaps of RMSE and improvement over the  $8 \times 8$  parameter grid.

The result is striking: the PG-EKF outperforms the standard EKF across the *entire* grid, with improvement never falling below 47% at the most extreme misspecification ( $\alpha_{\text{assumed}} = 1.5$ ,  $\beta_{\text{assumed}} = 0.5$ ). The maximum improvement (79%) occurs near the true parameters.

This robustness has a clear physical explanation: even with misspecified parameters, the

$\lambda_{\text{gate}}$  Robustness Analysis: Goldilocks Zone in Metastable Regime

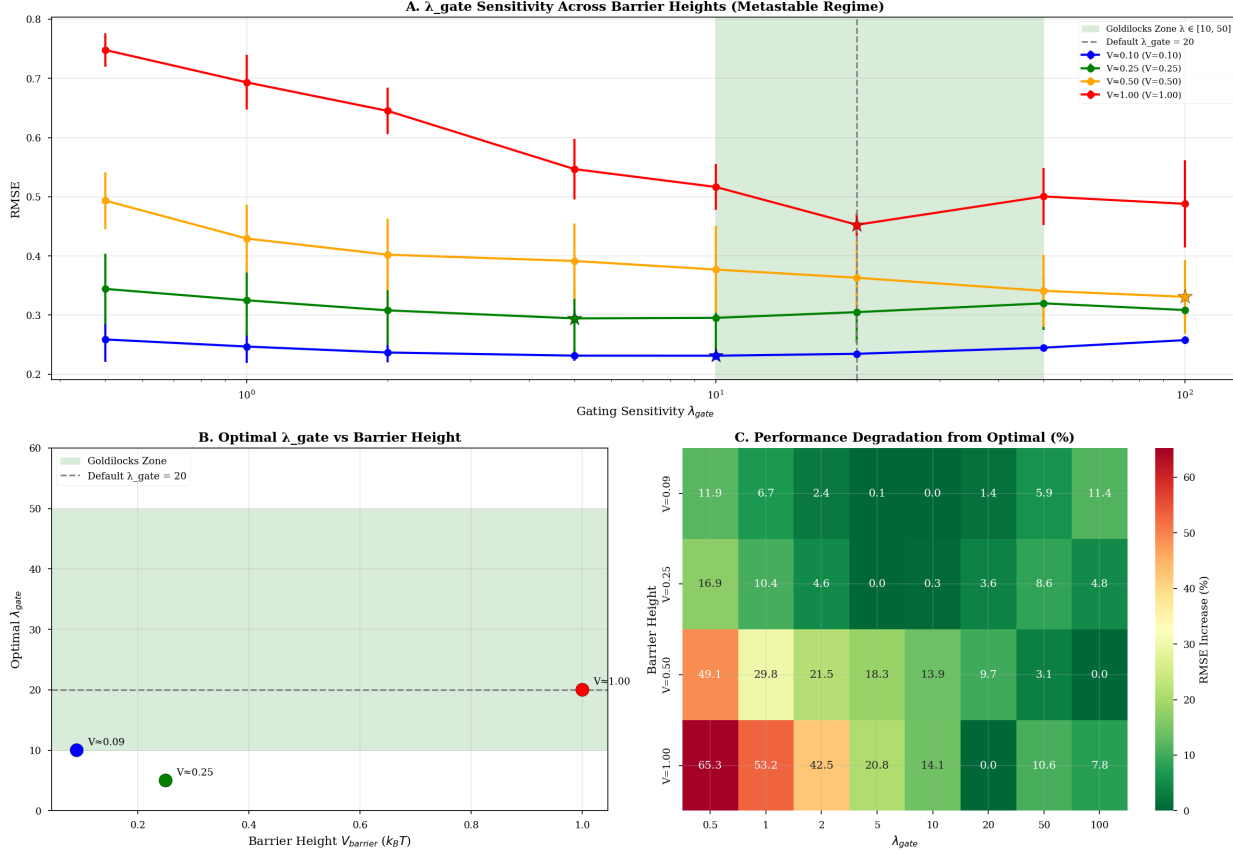


FIG. 3. Sensitivity of PG-EKF performance to hyperparameters  $\lambda$  and  $g$  across four potential topologies ( $\alpha = 0.6, 1.0, 1.41, 2.0$ ). A broad “Goldilocks zone” ( $\lambda \in [0.05, 0.5]$ ,  $g \in [5, 30]$ , shaded region) provides near-optimal RMSE reduction regardless of the specific potential shape. The robustness of this plateau means that approximate parameter knowledge is sufficient for effective gating.

GL potential preserves the correct topology (two wells separated by a barrier), and the gating mechanism continues to function because it depends on the *shape* of the energy landscape rather than its precise numerical parameters. The comparison with NT-EKF (57%) confirms that the continuous energy profile adds  $\sim 21$  percentage points of improvement beyond mere topological awareness, while also showing that the majority of the benefit is topological in nature. This decomposition—roughly two-thirds topology, one-third energy profile—provides a useful heuristic for practitioners: even a crude estimate of the potential topology is far better than no physics at all.

**C3: Model Misspecification Analysis**  
(True:  $\alpha=1.0$ ,  $\beta=1.0$ ;  $\square$  = true parameters)

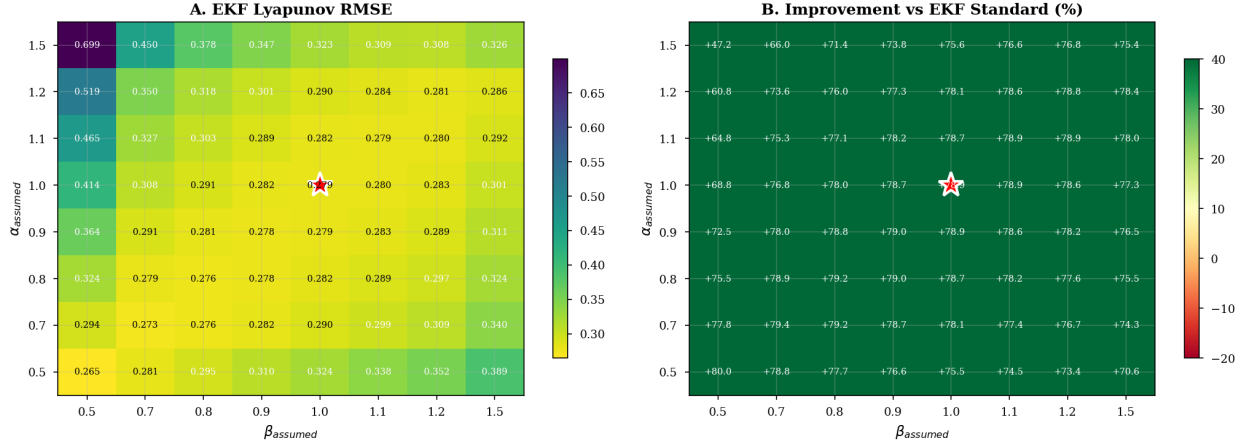


FIG. 4. Model misspecification analysis. Left: PG-EKF RMSE as a function of assumed potential parameters ( $\alpha_{\text{assumed}}, \beta_{\text{assumed}}$ ) when the true parameters are  $\alpha^* = \beta^* = 1.0$  (starred cell). Right: corresponding improvement over EKF Std. The improvement never falls below 47% across the entire grid, even at the most extreme misspecification ( $\alpha_{\text{assumed}} = 1.5$ ,  $\beta_{\text{assumed}} = 0.5$ ). This robustness arises because the GL potential preserves the correct topology (two wells separated by a barrier) regardless of the precise parameter values.

### E. Forced vs. spontaneous transitions

The synthetic benchmark uses externally forced transitions to ensure that both wells are visited within  $T = 300$  time steps. A natural concern is whether the gating mechanism also works for spontaneous, noise-induced (Kramers-type) transitions, which follow the energy landscape more closely than forced transitions.

We address this with a supplementary experiment using adapted parameters ( $\sigma = 0.50$ ,  $T = 2000$ ) that lower the Kramers barrier ratio to  $\Pi_1 = 2.0$ , yielding expected mean escape times of  $\tau_{\text{Kramers}} \approx 33$  time units. We run 20 replications and retain only those with at least two zero-crossings (9 out of 20; the low yield reflects the high variance inherent in exponentially distributed escape times). Figure 5 and Table II compare the three key filters under both transition mechanisms.

The PG-EKF shows moderate degradation from 78.9% to 67.7% under Kramers transitions—a relative loss of 14%, indicating that the gating mechanism is robust to the transition

### C6: Forced vs Kramers Transition Comparison

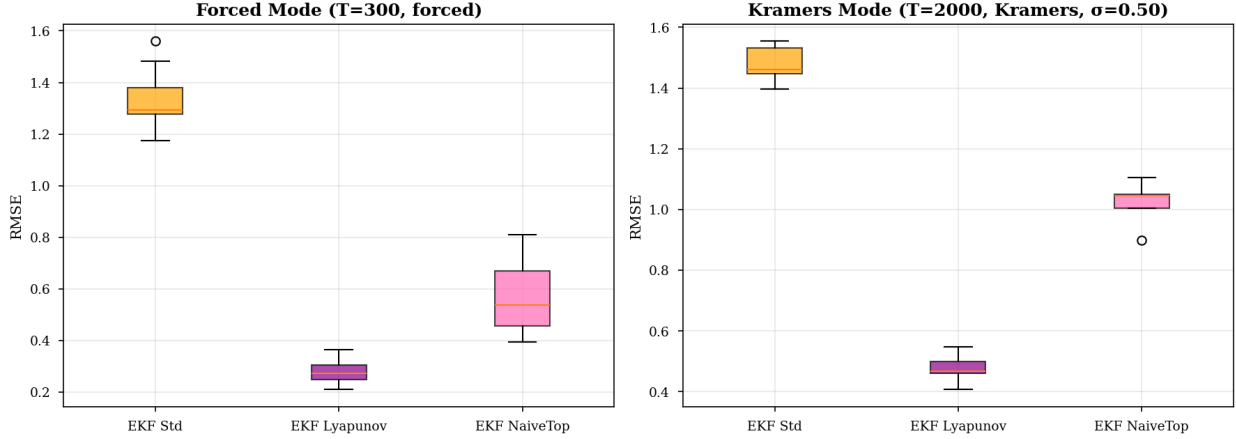


FIG. 5. RMSE distributions for EKF Std, PG-EKF, and NT-EKF under forced transitions (left,  $T = 300$ ,  $N_{\text{rep}} = 20$ ) and spontaneous Kramers transitions (right,  $\sigma = 0.50$ ,  $T = 2000$ ,  $N_{\text{rep}} = 9$  with  $\geq 2$  zero-crossings). Under Kramers transitions, the PG-EKF retains most of its advantage (+67.7%), while the NT-EKF degrades sharply (+30.3%), demonstrating that the continuous potential profile is most valuable precisely when transitions follow the physical energy landscape rather than external forcing.

TABLE II. Filter performance under forced vs. Kramers (spontaneous) transitions.  $N_{\text{rep}}$  is the number of usable replications. Improvement is relative to EKF Std within each mode.

| Mode                                | Filter  | RMSE  | Std   | Impr. (%) |
|-------------------------------------|---------|-------|-------|-----------|
| Forced<br>( $N_{\text{rep}} = 20$ ) | EKF Std | 1.324 | 0.094 | —         |
|                                     | PG-EKF  | 0.279 | 0.042 | +78.9     |
|                                     | NT-EKF  | 0.567 | 0.133 | +57.1     |
| Kramers<br>( $N_{\text{rep}} = 9$ ) | EKF Std | 1.476 | 0.056 | —         |
|                                     | PG-EKF  | 0.477 | 0.039 | +67.7     |
|                                     | NT-EKF  | 1.030 | 0.056 | +30.3     |

mechanism. The NT-EKF, by contrast, degrades dramatically from 57.1% to 30.3%—a relative loss of 47%. This asymmetry provides the strongest evidence for the value of the continuous potential profile: during spontaneous transitions, the system follows the energy landscape more closely than during forced transitions, and the PG-EKF exploits this struc-

ture while the NT-EKF, which knows only the well locations, cannot. The gap between PG-EKF and NT-EKF widens from 21 percentage points (forced) to 37 percentage points (Kramers), confirming that the energetic component of the gating becomes proportionally more important under physically realistic transition dynamics.

#### F. Data scarcity and outlier dependence

We evaluate performance across sample sizes  $N \in \{40, 50, 75, 100, 150, 200, 300\}$  and outlier fractions  $p \in \{0, 0.05, 0.10, 0.15, 0.20, 0.25, 0.30\}$ . The PG-EKF improvement increases monotonically with  $p$ , from  $\sim 3\%$  at  $p = 0$  (clean data) to  $\sim 80\%$  at  $p = 0.25$ . The method provides modest but positive improvement even on clean data, because the potential-energy penalty acts as a regularizer that prevents transient noise excursions from being interpreted as state changes. Performance is approximately constant across  $N$  for fixed  $p$ , confirming that the benefit is driven by outlier contamination rather than sample size.

### V. EMPIRICAL ILLUSTRATION: NGRIP ICE-CORE DATA

#### A. Data and preprocessing

As an empirical illustration, we apply the framework to the NGRIP  $\delta^{18}\text{O}$  ice-core record [29], which exhibits the characteristic bistable signature of Dansgaard-Oeschger (D-O) events: rapid warmings (stadial-to-interstadial transitions) followed by gradual coolings (Fig. 6).

We analyze 19 D-O events, each segmented around the transition with  $N = 226$  data points covering the interstadial phase. The data are normalized bimodally: we identify the stadial and interstadial modes of the  $\delta^{18}\text{O}$  distribution and center the data at their midpoint, scaling by their separation. In normalized coordinates, the two modes lie near  $x = \pm 1$ .

#### B. Asymmetry estimation

For each D-O event, we estimate the asymmetry parameter  $\gamma$  by fitting the asymmetric GL potential (Eq. 4) to the local distribution. Across 19 events, we obtain a median  $\hat{\gamma} = -0.109$  with standard deviation 0.228, indicating that the stadial (cold) well is deeper than

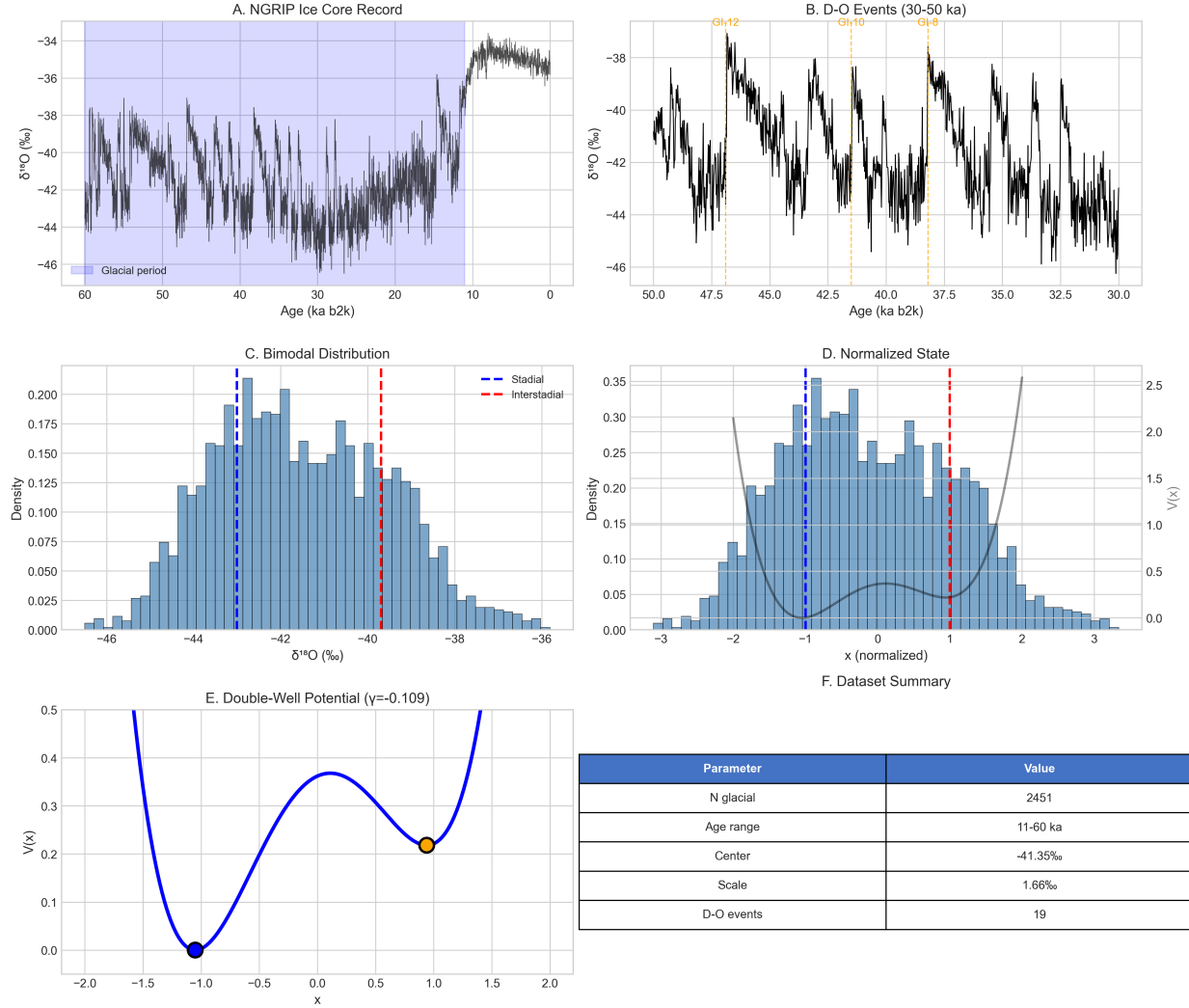


FIG. 6. The NGRIP  $\delta^{18}\text{O}$  ice-core record showing Dansgaard-Oeschger events over the last glacial period. The data exhibit the characteristic bistable pattern: rapid warmings (stadial  $\rightarrow$  interstadial) followed by gradual coolings. Vertical markers indicate the 19 D-O events used for asymmetry estimation and filter validation.

the interstadial (warm) well—consistent with the observation that stadial periods are longer-lived than interstadial periods in the NGRIP record.

We assess the significance of this asymmetry with four complementary tests: a one-sample  $t$ -test ( $t = -2.15, p = 0.045$ ); a Wilcoxon signed-rank test ( $W = 48, p = 0.060$ ); a sign test (12/19 negative,  $p = 0.359$ ); and a nonparametric bootstrap 95% CI ( $[-0.220, -0.011]$ , 10,000 replications, percentile method).

The  $t$ -test is marginally significant at the 5% level; the Wilcoxon test is significant at

### Validation: Ginzburg-Landau Assumption via Boltzmann Inversion

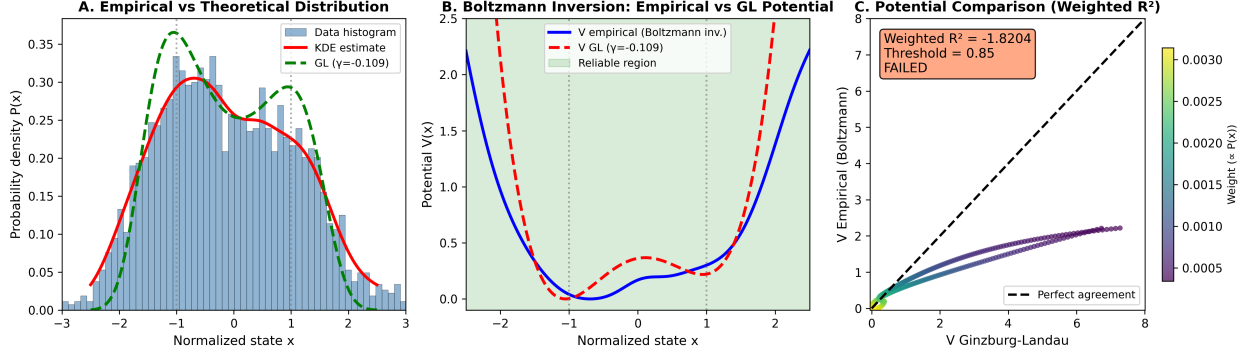


FIG. 7. Validation of the Ginzburg-Landau assumption on NGRIP data. Left: empirical probability density (histogram and KDE) vs. GL prediction ( $\gamma = -0.109$ ). Center: empirical potential from Boltzmann inversion vs. GL quartic form; the shaded region marks the inter-well zone where the two agree reasonably. Right: weighted  $R^2$  comparison, yielding  $R^2 = -1.82$  (below the 0.85 threshold). The GL potential fails as a global fit but captures the local topology (two wells, one barrier) that the gating mechanism requires.

the 10% but not the 5% level; the sign test, which discards magnitude information, lacks power at  $n = 19$ . The bootstrap CI excludes zero, providing the strongest nonparametric evidence for a non-zero asymmetry. We characterize the evidence as moderate: consistent across methods but not overwhelming given the small sample size.

### C. Ginzburg-Landau validation

Before applying the gating framework, we test how well the quartic GL potential approximates the effective potential of the NGRIP system. We reconstruct the empirical potential via Boltzmann inversion ( $V_{\text{emp}} = -T_{\text{eff}} \ln P_{\text{emp}}$ ) and compare it with the fitted GL form (Fig. 7).

The weighted  $R^2$  between the two potentials is  $-1.82$ , indicating that the quartic GL polynomial provides a poor *global* fit to the empirical potential. This negative result deserves careful interpretation. The GL potential is a minimal model capturing bistability and asymmetry; it is not intended to reproduce the full complexity of the empirical potential, which may include higher-order terms, non-polynomial features, and non-Markovian effects [18]. The relevant question for our framework is not whether the GL potential accurately rep-

TABLE III. PG-EKF improvement (%) on NGRIP data ( $\hat{\gamma} = -0.109$ , 20 MC replications). Values are mean  $\pm$  SE. At 0% outlier, SE = 0 because the same clean trajectory produces identical filter output.

| $N$ | 0%    | 2%              | 5%              | 10%             | 15%             |
|-----|-------|-----------------|-----------------|-----------------|-----------------|
| 226 | +12.4 | +28.3 $\pm$ 1.8 | +42.2 $\pm$ 1.9 | +48.0 $\pm$ 1.5 | +52.3 $\pm$ 1.4 |
| 113 | +12.7 | +31.7 $\pm$ 2.0 | +40.5 $\pm$ 1.9 | +46.3 $\pm$ 1.8 | +50.0 $\pm$ 1.8 |
| 76  | +1.0  | +20.4 $\pm$ 3.0 | +37.9 $\pm$ 2.4 | +48.8 $\pm$ 2.4 | +52.3 $\pm$ 2.1 |
| 57  | +22.8 | +38.4 $\pm$ 3.5 | +44.5 $\pm$ 2.9 | +48.2 $\pm$ 2.3 | +52.3 $\pm$ 2.3 |
| 46  | +12.1 | +26.4 $\pm$ 3.6 | +36.2 $\pm$ 3.2 | +44.4 $\pm$ 2.2 | +48.0 $\pm$ 2.2 |

resents the global energy landscape, but whether it captures the local topology—two wells separated by a barrier—sufficiently well to enable effective gating. The misspecification analysis of Sec. IV D demonstrates that the gating mechanism is robust to substantial parametric errors, and the results below confirm significant improvement on NGRIP data despite the imperfect GL fit.

#### D. Filter performance on NGRIP data

We evaluate the PG-EKF and PG-PF (along with their standard counterparts) on the normalized NGRIP data with 20 Monte Carlo replications per condition, varying the synthetic outlier contamination injected into the real data to create a controlled benchmark. Table III reports the EKF results with standard errors and 95% confidence intervals.

Figure 8 illustrates the filtering behavior on a representative D-O event, showing how the PG-EKF tracks the true state through the transition while the standard EKF is corrupted by outliers.

The improvement is driven primarily by the outlier fraction: a two-way ANOVA on the EKF improvement surface shows that outlier fraction explains 91.1% of the total variance ( $F_{5,20} = 78.0$ ,  $p = 2 \times 10^{-12}$ ), while sample size explains only 4.2% ( $F_{4,20} = 4.5$ ,  $p = 0.009$ ). This confirms the framework’s principal mechanism: physics-based gating is most valuable when observations are contaminated, regardless of sample size.

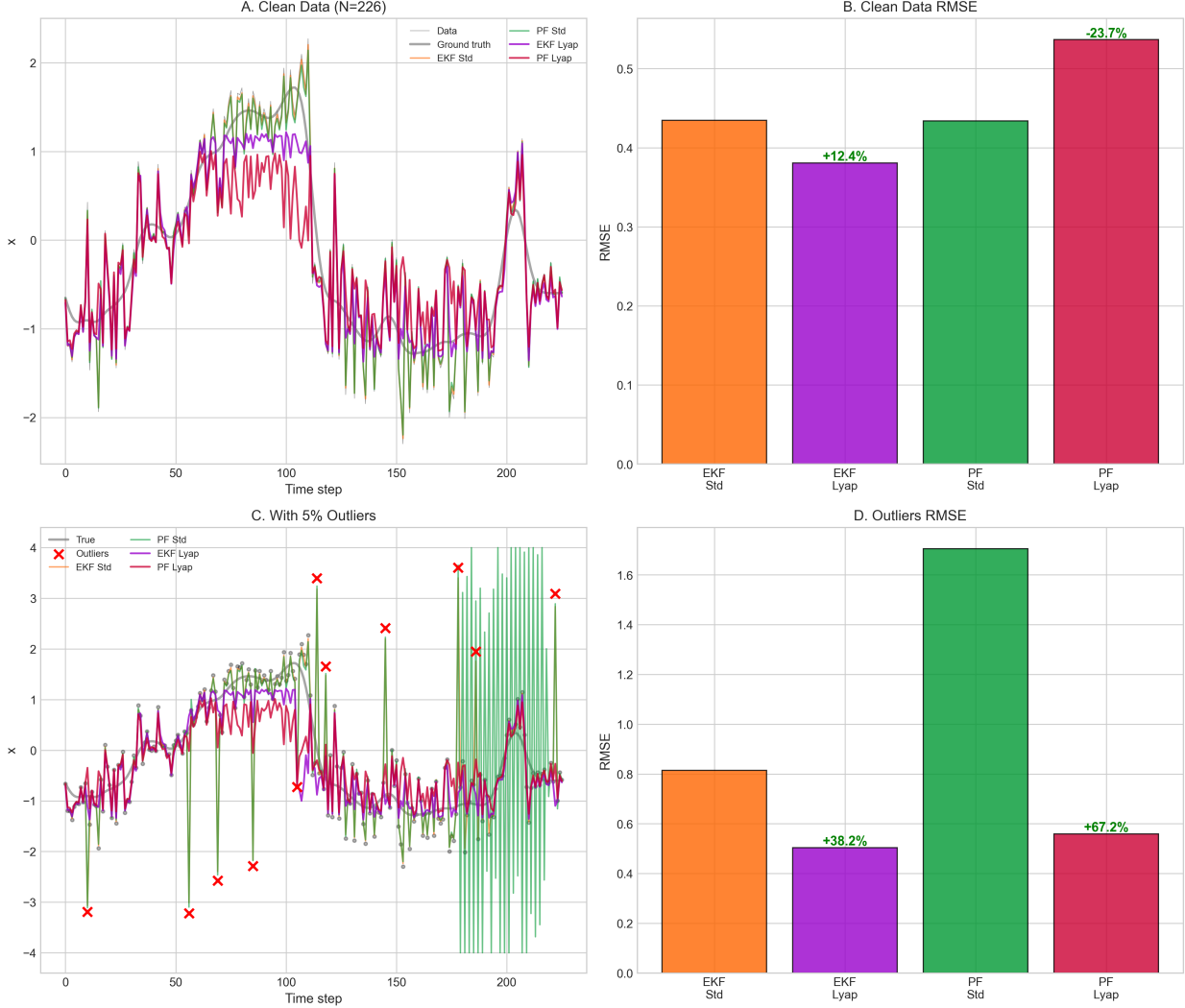


FIG. 8. PG-EKF and PG-PF performance on NGRIP data (D-O event GI-8,  $N = 226$ ). Top row: clean data—the PG-EKF provides a modest +12.4% improvement; the PG-PF degrades by −23.7% due to over-regularization (see Sec. V E). Bottom row: 5% outlier contamination—both potential-gated filters substantially outperform their standard counterparts, with the PG-PF achieving +67.2% improvement by effectively ignoring outliers via the energy-modulated likelihood.

### E. Particle filter behavior on clean data

An important caveat concerns the PG-PF on clean data ( $p = 0$ ). At  $N = 226$ , the PG-PF shows a −23.4% degradation relative to the standard PF, worsening to −53.1% at  $N = 76$ . This occurs because the potential-energy gating introduces a systematic bias in the particle weights: particles near well minima receive disproportionately high weight even

when no outliers are present, effectively over-regularizing the posterior. The PG-PF should therefore be used only when outlier contamination is expected ( $p \gtrsim 5\%$ ), at which point it outperforms all other methods (reaching +61.6% improvement at 15% contamination with  $N = 226$ ).

## VI. DISCUSSION

### A. What is new and what is not

The use of double-well potentials for modeling bistable dynamics is well established [2, 4]. The use of Kalman filters for parameter estimation in such systems has been developed by Kwasniok and collaborators [14, 15]. The use of robust filtering to handle outliers has a long history in tracking [8] and signal processing [10, 12].

What is new is the combination: using the potential energy landscape to modulate the observation noise covariance in real time. This places physics in a channel—observation reliability—where it has not previously appeared in the Bayesian filtering literature. Constrained filters [19] impose physics on states; PINNs [20] impose physics on loss functions during training; adaptive  $R$  estimation [23] learns  $R$  from innovation statistics. Chang [9] inflates  $R$  when an observation fails a Mahalanobis distance test, which is the closest existing mechanism in functional form, but the trigger is statistical rather than physical. Our approach is orthogonal to all of these: it prescribes  $R$  from a physical model rather than inferring it from data.

### B. The topological vs. energetic decomposition

The comparison between PG-EKF (78.2% improvement) and NT-EKF (57.0%) decomposes the benefit into two components: 57 percentage points from topology (knowing where the wells are) and 21 percentage points from energy (knowing the shape of the potential between the wells). The Kramers experiment sharpens this decomposition: under spontaneous transitions, the energetic component becomes proportionally more important (PG-EKF 67.7% vs. NT-EKF 30.3%, a gap of 37 percentage points rather than 21). This suggests that the full potential profile is most valuable precisely when it is most physically relevant: during transitions governed by the energy landscape rather than external forcing.

### C. Limitations

*a. Residual autocorrelation.* The Hessian-based covariance (Eq. 11) produces residuals with significant autocorrelation at lags 1–6, more pronounced than in the standard EKF. This indicates that the posterior is slightly over-confident: the regularization term smooths the state estimate, creating temporal correlations in the prediction errors. In the present context of outlier rejection, this over-confidence is a favorable trade-off (better point estimates at the cost of miscalibrated uncertainty), but applications requiring accurate posterior uncertainty quantification should consider inflating  $P^+$  by a small factor or replacing the Hessian-based update with an inflation-corrected variant.

*b. Known potential assumption.* The method requires specification of the potential parameters  $(\alpha, \beta, \gamma)$ . The misspecification analysis (Sec. IV D) shows robustness to errors up to 50%, and the required information is topological (number and approximate location of wells) rather than precise. In many applications, this information is available from domain knowledge or preliminary data analysis. Nevertheless, the assumption limits direct applicability to systems where bistability is known *a priori*.

*c. Scalar state.* The present formulation is restricted to scalar state variables. Extension to multivariate systems is conceptually straightforward—replace  $V(x)$  with a multivariate potential and  $R$  with a state-dependent matrix—but raises computational cost questions and requires meaningful definitions of multivariate potential landscapes.

*d. GL potential mismatch.* The Boltzmann validation on NGRIP data yields  $R^2 = -1.82$  (Sec. V C), confirming that the quartic GL potential is not the true effective potential of the climate system. The framework functions despite this mismatch because the gating mechanism depends on the topology (wells and barrier) rather than the global potential shape. Better-fitting potentials (higher-order polynomials, nonparametric forms) could provide additional improvement.

## VII. CONCLUSION

We have introduced potential-energy gating, a method that uses the energy landscape of a bistable system to modulate the observation noise covariance of a Bayesian filter. The method is simple to implement (two additional hyperparameters), architecture-agnostic

(demonstrated across five filter families), robust to parameter misspecification (improvement  $> 47\%$  even with 50% parameter errors), and effective on both synthetic and empirical data.

The key insight is that in bistable systems, observation reliability is not spatially uniform: measurements near potential well minima carry more information than measurements near the barrier. Encoding this physics in the observation model produces large and statistically robust improvements in state estimation accuracy, outperforming both purely statistical approaches (chi-square gating, Student- $t$  filters) and purely topological approaches (naive distance-based gating).

The method is applicable to any system where the existence and approximate location of metastable states can be specified *a priori* from domain knowledge, experimental evidence, or preliminary data analysis. Natural extensions include multivariate state spaces, online estimation of potential parameters, and coupling with data-driven methods for systems where the potential form is not known analytically.

Code and data are available from the author upon reasonable request.

## ACKNOWLEDGMENTS

The author thanks the North Greenland Ice Core Project members for making the ice-core data publicly available.

---

- [1] H. Haken, *Synergetics: Introduction and Advanced Topics*, 3rd ed. (Springer, Berlin, 1983).
- [2] H. A. Kramers, *Physica* **7**, 284 (1940).
- [3] C. Gardiner, *Stochastic Methods: A Handbook for the Natural and Social Sciences*, 4th ed. (Springer, Berlin, 2009).
- [4] P. D. Ditlevsen, *Geophys. Res. Lett.* **26**, 1441 (1999).
- [5] J. D. Hamilton, *Econometrica* **57**, 357 (1989).
- [6] R. E. Kalman, *J. Basic Eng.* **82**, 35 (1960).
- [7] S. Särkkä, *Bayesian Filtering and Smoothing* (Cambridge University Press, Cambridge, 2013).
- [8] Y. Bar-Shalom, X. R. Li, and T. Kirubarajan, *Estimation with Applications to Tracking and*

*Navigation* (Wiley, New York, 2001).

[9] G. Chang, J. Geodesy **88**, 391 (2014).

[10] G. Agamennoni, J. I. Nieto, and E. M. Nebot, IEEE Trans. Signal Process. **60**, 5024 (2012).

[11] M. Roth, E. Özkan, and F. Gustafsson, in *Proc. IEEE ICASSP* (Vancouver, 2013) pp. 5770–5774.

[12] M. Roth, T. Ardeshiri, E. Özkan, and F. Gustafsson, arXiv preprint arXiv:1703.02428 (2017).

[13] H. A. P. Blom and Y. Bar-Shalom, IEEE Trans. Autom. Control **33**, 780 (1988).

[14] F. Kwasniok and G. Lohmann, Phys. Rev. E **80**, 066104 (2009).

[15] F. Kwasniok, Phys. Rev. E **86**, 036214 (2012).

[16] V. N. Livina, F. Kwasniok, and T. M. Lenton, Clim. Past **6**, 77 (2010).

[17] V. N. Livina and T. M. Lenton, Geophys. Res. Lett. **34**, L03712 (2007).

[18] J. Lohmann and P. D. Ditlevsen, Clim. Dyn. **52**, 6411 (2019).

[19] D. J. Simon, IET Control Theory Appl. **4**, 1303 (2010).

[20] M. Raissi, P. Perdikaris, and G. E. Karniadakis, J. Comput. Phys. **378**, 686 (2019).

[21] G. E. Karniadakis, I. G. Kevrekidis, L. Lu, P. Perdikaris, S. Wang, and L. Yang, Nat. Rev. Phys. **3**, 422 (2021).

[22] S. L. Brunton, J. L. Proctor, and J. N. Kutz, Proc. Natl. Acad. Sci. U.S.A. **113**, 3932 (2016).

[23] P. Tandeo, P. Ailliot, M. Bocquet, A. Carrassi, T. Miyoshi, M. Pulido, and Y. Zhen, Mon. Weather Rev. **148**, 3973 (2020).

[24] V. L. Ginzburg and L. D. Landau, Zh. Eksp. Teor. Fiz. **20**, 1064 (1950).

[25] R. H. Byrd, P. Lu, J. Nocedal, and C. Zhu, SIAM J. Sci. Comput. **16**, 1190 (1995).

[26] S. J. Julier and J. K. Uhlmann, Proc. IEEE **92**, 401 (2004).

[27] G. Evensen, Ocean Dyn. **53**, 343 (2003).

[28] N. J. Gordon, D. J. Salmond, and A. F. M. Smith, IEE Proc. F **140**, 107 (1993).

[29] North Greenland Ice Core Project members, Nature **431**, 147 (2004).